

Article

# Hardness, Young's Modulus and Elastic Recovery in Magnetron Sputtered Amorphous AlMgB<sub>14</sub> Films

Alexander M. Grishin <sup>1,2,3</sup> 

<sup>1</sup> Division of Electronics and Embedded Systems, School of Electrical Engineering and Computer Science, KTH Royal Institute of Technology, SE-164 40 Stockholm-Kista, Sweden; grishin@kth.se; Tel.: +46-8-790-4176

<sup>2</sup> INMATECH Intelligent Materials Technology, SE-127 51 Skärholmen, Sweden

<sup>3</sup> Petrozavodsk State University, 185910 Petrozavodsk, Russia

Received: 24 August 2020; Accepted: 15 September 2020; Published: 16 September 2020



**Abstract:** We report optical and mechanical properties of hard aluminum magnesium boride films magnetron sputtered from a stoichiometric AlMgB<sub>14</sub> ceramic target onto Corning® 1737 Glass and Si (100) wafers. High target sputtering rf-power and sufficiently short target-to-substrate distance appeared to be critical processing conditions. Amorphous AlMgB<sub>14</sub> films demonstrate very strong indentation size effect (ISE): exceptionally high nanohardness  $H = 88$  GPa and elastic Young's modulus  $E^* = 517$  GPa at 26 nm of the diamond probe penetration depth and almost constant values, respectively, of about 35 GPa and 275 GPa starting at depths of about 2–3% of films' thickness. For comparative analysis of elastic strain to failure index  $H/E^*$ , resistance to plastic deformation ratio  $H^3/E^{*2}$  and elastic recovery ratio  $W_e$  were obtained in nanoindentation tests performed in a wide range of loading forces from 0.5 to 40 mN. High authentic numerical values of  $H = 50$  GPa and  $E^* = 340$  GPa correlate with as low as only 10% of total energy dissipating through the plastic deformations.

**Keywords:** optical refractive index and extinction coefficient; Raman icosahedral boron–boron vibrations; elastic and plastic energies; hardness; Young's modulus

## 1. Introduction

For the first time, aluminum magnesium boride was sintered in 1970 in Carborundum Company by V.I. Matkovich and J. Economy. Small black AlMgB<sub>14</sub> crystals were prepared by heating a mixture of aluminum, magnesium and boron at a temperature of 900 °C. Their structure was determined as a 3D network formed from icosahedral B<sub>12</sub> groups within the orthorhombic unit cell with the dimensions  $a = 10.313$  Å,  $b = 8.115$  Å, and  $c = 5.848$  Å [1]. Results obtained in succeeding works on AlMgB<sub>14</sub> can be divided into three main groups. True stoichiometry Al<sub>0.75</sub>Mg<sub>0.78</sub>B<sub>14</sub>, thermoelectric, electronic and optical properties were reported between the 1970s and 1990s (see references in Ref. [2]). Next, in 1993 Higashi et al. and later in 2000 Cook et al. from Iowa have reported exceptional hardness of AlMgB<sub>14</sub> crystals as high as, respectively, 27.4–28.3 GPa [3] and 32–35 GPa [2]. Lastly in 2003, the same Iowa group took an important step in exploration of AlMgB<sub>14</sub> fabricating superhard self-lubricating (hereinafter BAM) films. They used pulsed laser deposition (PLD) technique to obtain films which hardness ranged from 45 to 51 GPa [4].

Recently, we succeeded in deposition of high quality amorphous BAM films by an RF magnetron sputtering method which can easily be scaled up for industrial use. High sputtering power of ceramic AlMgB<sub>14</sub> target, moderately low substrate temperature, and a short target-to-substrate distance enabled high-energy ballistic impact regime of adatoms' motion thus leading to an enhanced hardness by 25% and Young's modulus by 60%, compared to PLD-made films. Correct stoichiometry and compositional in-depth homogeneity governed superior mechanical properties of magnetron sputtered films [5]. Correlative theoretical and experimental elaboration of high power pulsed magnetron sputtering

(HPPMS) of  $\text{AlYB}_{14}$  films acknowledged the ability to form icosahedral boron-rich phases below the bulk synthesis temperatures [6]. Matching results of ab initio molecular dynamics calculations of elastic properties with nanoindentation measurements of Young's modulus proved the predictive power of the HPPMS technique to sinter amorphous boride coatings [7].

Both amorphous  $\text{AlMgB}_{14}$  films obtained by pulsed laser deposition [4] and magnetron sputtering [5] exhibit a strong indentation size effect (ISE). This is the exceptionally high parameters of nanohardness  $H$  and elastic Young's modulus  $E^*$  at the tens-of-nanometer-scale of penetration depth of a diamond probe and their very steep decrease to the constant values at depths of about 2–3% of the film's thickness. Still the general necessity remains to authenticate these results. Herein, we examined additional mechanical parameters: elastic strain to failure index  $H/E^*$ , resistance to plastic deformation ratio  $H^3/E^{*2}$ , and elastic recovery ratio  $W_e$ . Maximum values of calculated parameter  $H^3/E^{*2}$  and measured  $W_e$  as high as 90% always match the peak values of hardness  $H$  and elastic modulus  $E^*$ . Therefore, we relate ISE to a very low portion of total energy dissipating through the plastic deformations at shallow indenter prints.

## 2. Materials and Methods

The details of RF magnetron sputtering of ultra-hard  $\text{AlMgB}_{14}$  coatings were published elsewhere [5]. In brief, a batch of BAM films was deposited onto Si(100) wafers and Corning® 1737 glass by sputtering of a stoichiometric  $\text{AlMgB}_{14}$  ceramic target. The target was manufactured via the grinding and subsequent spark plasma sintering of Al (99.97%), Mg (99.8%), and B (99%) powders [8]. The ultimate pressure in vacuum chamber was better than  $3 \times 10^{-7}$  Torr, films deposition was carried out at 7 mTorr of Ar-gas pressure. In-depth uniformity, smooth surface and ultimate hardness of BAM films were achieved at optimum processing conditions: distance of 25 mm between 1 inch 50 W RF powered magnetron and substrates kept on the heater at 250–350 °C. Typical film size was  $10 \times 10 \text{ mm}^2$ , deposition rate was 0.44 nm/s. Films' roughness was checked with KLA-Tencor P-15 stylus profiler. It does not exceed the roughness of Corning® 1737 glass and Si wafers as the substrates.

All films sintered at different temperatures varied from room temperature up to 550 °C and appeared to be X-ray amorphous. BAM films onto Si wafers do not exhibit themselves with any XRD pattern (recorded with a Siemens D-5000 powder diffractometer) even in a magnifying log-scale.  $\Theta$ - $2\Theta$  scan of 0.4  $\mu\text{m}$  thick BAM/Si film in the main frame of Figure 1 contains only Si(100) wafer's Bragg reflections. In insets, the selected area electron diffraction (SAED, performed on a FEI Tecnai T20 TEM) pattern and HRTEM image also attest amorphous structure of 2.12- $\mu\text{m}$ -thick BAM/Si film.

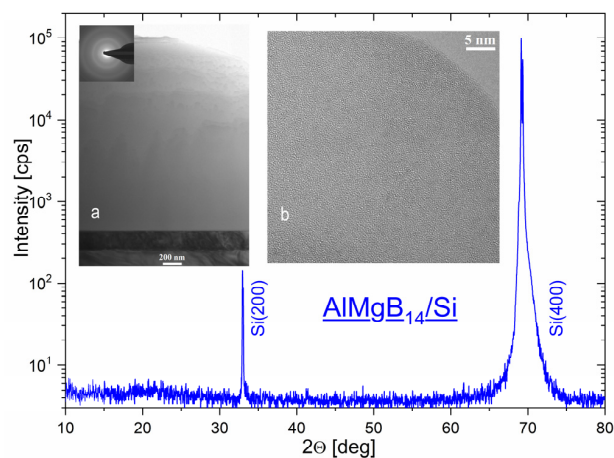


**Figure 1.** Main frame  $\text{CuK}\alpha$  radiation of 0.4- $\mu\text{m}$ -thick  $\text{AlMgB}_{14}$  film magnetron sputtered onto Si(100) wafer at 550 °C. Insets—XRD  $\Theta$ - $2\Theta$  scan in ts: **a**—SAED pattern and **b**—high resolution TEM image of RF15-2(2.12  $\mu\text{m}$ )  $\text{AlMgB}_{14}$  film grown onto Si(100) at 250 °C. Electron microscopy images provided courtesy of Dr. Jun Lu.

Optical dispersion was evaluated from the transmission spectrum of BAM films onto glass substrate recorded at normal light incidence with a Fourier transform infrared spectrometer *Nicolet 5700* in the range 0.3–2.5  $\mu\text{m}$ . The spectrum was normalized to the spectrum of the bare glass substrate. Unpolarized backscattered micro-Raman spectra of  $\text{AlMgB}_{14}$  films onto Si(100) wafers were collected with a confocal Thermo Scientific Nicolet Almega XR Dispersive Raman Spectrometer at room temperature using 785 nm and 532 nm laser pumping. NHT S/N 06-0134 and TTX-NHT2 S/N 01-05821 nanoindentation instruments with Berkovich three-sided diamond pyramid tips were employed to measure hardness  $H$  and effective Young's modulus  $E^* = E/(1 - \nu^2)$ . In calculation we used  $\nu = 0.25$  as a Poisson's ratio for  $\text{AlMgB}_{14}$  films. Abrasion BAM films' properties were characterized using CSM Instruments SA micro-scratch tester S/N 01-03079 with the diamond Rockwell C indenter of 200- $\mu\text{m}$  radius.

### 3. Results and Discussion

#### 3.1. Optical Properties

Circular symbols in Figure 2 display optical transmission spectrum of 0.53- $\mu\text{m}$ -thick film onto transparent Corning<sup>®</sup> 1737 glass substrate. It has a semiconductor-type character. The absorption edge lies around 310 nm (bandgap is 4 eV) and specific resistivity  $\rho = 1 \Omega \text{ cm}$ .

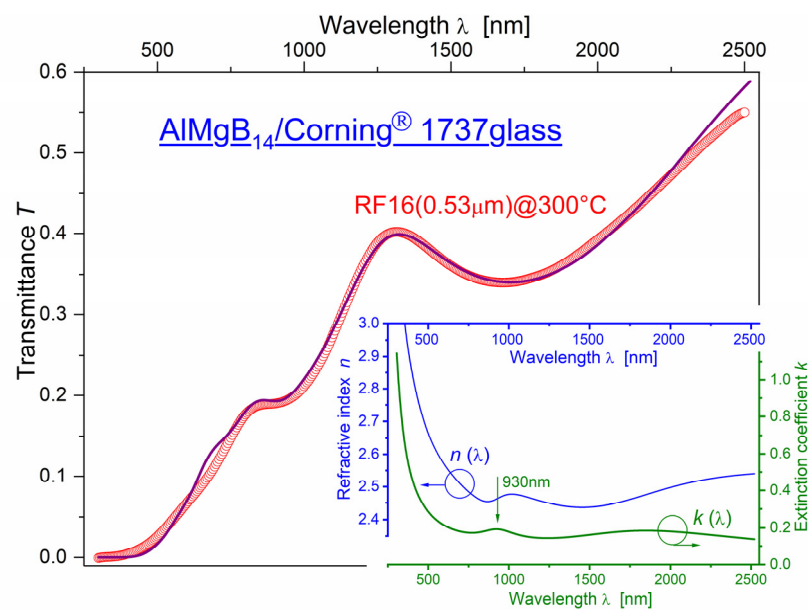


**Figure 2.** Circular red color symbols show experimental optical transmittance  $T(\lambda)$  in 0.53- $\mu\text{m}$ -thick  $\text{AlMgB}_{14}$  film grown at 300 °C onto the Corning<sup>®</sup> 1737 glass substrate. Solid lines in the main frame and inset depict, respectively, theoretical  $T(\lambda)$ , refractive index  $n(\lambda)$  and extinction coefficient  $k(\lambda)$  simulated with the Swanepoel formula (see Appendix A) and Equation (1) for complex refractive index accounting for three electric dipole resonances.

Observed spectrum features we modeled with a commonly used Swanepoel [9] formula (follows afterward in Appendix A). Theoretical solid line in Figure 2 firmly fits to the experimental spectrum. A good agreement with the experimental results was achieved presenting complex refractive index with three Sellmeier-type electric dipole resonances, Equation (1):

$$\begin{aligned}
 (n - ik)^2 = 1 + & \frac{4.85}{1 - (270\text{nm}/\lambda)^2 + i \times 0.34(270\text{nm}/\lambda)} \\
 & + \frac{0.1}{1 - (930\text{nm}/\lambda)^2 + i \times 0.3(930\text{nm}/\lambda)} \\
 & + \frac{0.5}{1 - (1800\text{nm}/\lambda)^2 + i \times 0.8(1800\text{nm}/\lambda)}
 \end{aligned} \quad (1)$$

Inset to Figure 2 shows a wavelength dispersion of refractive index  $n(\lambda)$  and extinction coefficient  $k(\lambda)$  calculated with Equation (1). Within the explored 0.3–2.5  $\mu\text{m}$  range, they distinctly reveal dipole resonance at 930 nm. It manifests itself as a hump in extinction coefficient  $k(\lambda)$  and as a derivative-type curve of the real part of refractive index  $n(\lambda)$  correspondent to Kramers–Kronig relations.

Figure 3 presents unpolarized backscattered micro-Raman spectra for two RF15-2(2.12  $\mu\text{m}$ ) and RF11(0.88  $\mu\text{m}$ ) BAM films prepared onto Si(100), respectively, at 250  $^\circ\text{C}$  and 300  $^\circ\text{C}$ . Red/magenta and green/cyan color symbols depict spectra obtained at 785 nm and 532 nm laser light pumping, correspondingly.

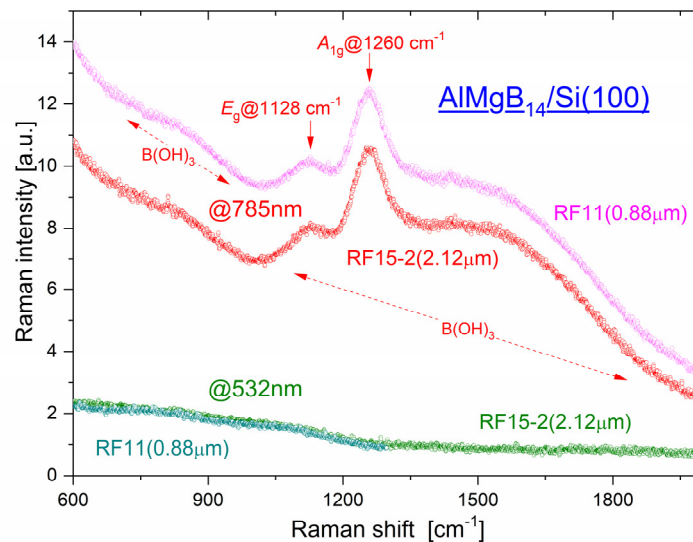


**Figure 3.** Unpolarized backscattered Raman spectra of two RF15-2(2.12  $\mu\text{m}$ ) and RF11(0.88  $\mu\text{m}$ ) AlMgB<sub>14</sub> films grown onto Si(100) wafers, respectively, at 250  $^\circ\text{C}$  and 300  $^\circ\text{C}$ . Excitations at 785 nm (1.58 eV) and 532 nm (2.33 eV) laser light pumping are shown with red/magenta and green/cyan colors, correspondingly. Two vertical arrows mark Raman intra-icosahedral B-B vibration  $E_g$  band at 1128  $\text{cm}^{-1}$  and inter-icosahedral B-B vibration  $A_{1g}$  modes at 1260  $\text{cm}^{-1}$ . Raman and IR active vibrations in the molecule of orthorhombic boric acid B(OH)<sub>3</sub> build the shoulder around 840  $\text{cm}^{-1}$  and a broad 1030–2000  $\text{cm}^{-1}$  band.

Since the structure of AlMgB<sub>14</sub> films is completely amorphous, the Raman spectra do not contain any narrow lines. There are two broad bands with maxima at 1128  $\text{cm}^{-1}$  and 1260  $\text{cm}^{-1}$ . Following Ref. [10] we attribute them, respectively, to intra-icosahedral B-B vibration  $E_g$  modes and to predominantly inter-icosahedral B-B vibration  $A_{1g}$  modes. The shoulder around 840  $\text{cm}^{-1}$  and the broad band ranging from 1030 up to 2000  $\text{cm}^{-1}$  can rely upon Raman and IR active vibrations in the molecule of orthorhombic boric acid [11]. Molecular vibrations of boric acid together with  $E_g$  and  $A_{1g}$  icosahedral B-B vibrational modes can be ascribed to the subtle optical resonance absorption at  $\lambda = 930$  nm revealed in inset to Figure 2.

Three (OH)<sup>−1</sup> groups surround B<sup>3+</sup> atom and form a planar trigonal molecular configuration. Strong hydrogen bonds between hydroxyl groups build a stable layer of B(OH)<sub>3</sub> molecules whereas only weak van der Waal's forces link two adjacent layers to each other at the distance of 0.318 nm. Easily sheared multilayered B(OH)<sub>3</sub> structure governs unique lubrication properties of crystalline

boric acid [12]. These nanometer-thick  $B(OH)_3$  surface layers make BAM films slicker than Teflon<sup>TM</sup> [13]. Mechanical properties of  $AlMgB_{14}$  films are not affected by boric acid since its hardness and elastic modulus are as low as 1.2 GPa and 15 GPa, correspondingly [14]. Due to ultra-high hardness and slipperiness, BAM films have great potential for a wide range of diverse applications for MEMS devices, wear-resistant and low-friction transparent coatings, metal dies, measuring tools and gauges.

### 3.2. Nanoindentation

Nanoindentation tests of  $AlMgB_{14}$  films on Si(100) wafers were conducted applying a load to Berkovich diamond pyramid tip from 0.5 up to 40 mN. The measurements were carried out applying a multiple simple matrix  $2 \times 2$  indentations to exclude spurious notches and collect reliable data sufficient for statistical averaging. A new diamond probe adjustment was performed every time for the next  $2 \times 2$  indentations. To eliminate a role of Si substrate, penetration depth of the diamond indenter did not exceed 10–15% of films' thickness. Typical loading  $L(h)$  (ascending) and unloading  $L_{\downarrow}(h)$  (descending) force curves are shown in Figure 4. The area between the loading and unloading curve represents the energy dissipated in BAM film due to plastic deformation whereas the area under the unloading curve defines recovered work of elastic forces.

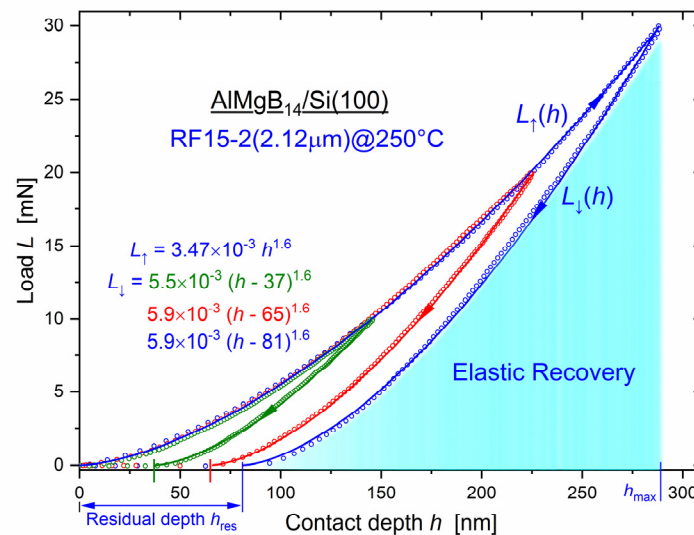


**Figure 4.** Load-displacement curves of the hard RF15-2(2.12  $\mu\text{m}$ )  $AlMgB_{14}$  film grown onto Si(100) substrate at 250  $^{\circ}\text{C}$ . Solid lines fit loading  $L_{\uparrow}(h)$  (ascending) and unloading  $L_{\downarrow}(h)$  (descending) experimental data shown with symbols. Area between  $L_{\uparrow}(h)$  and  $L_{\downarrow}(h)$  curves corresponds to plastic deformations whereas the colored section depicts the area of elastic recovery.

Load-displacement curves are used to determine three main parameters that characterize hard  $AlMgB_{14}$  films: hardness  $H$ , effective Young's modulus  $E^* = E/(1 - \nu^2)$  and elastic recovery ratio  $W_e$ .  $H$  and  $E^*$  are calculated as per the Oliver and Pharr method fitting  $L_{\downarrow}(h) = A(h - h_{\text{res}})^m$  dependence to the experimental unloading force curve [15]. Elastic recovery ratio is defined as a ratio of areas under unloading  $L_{\downarrow}(h)$  and loading  $L_{\uparrow}(h)$  curves, Equation (2):

$$W_e = \int_{h_{\text{res}}}^{h_{\text{max}}} dh \cdot L_{\downarrow}(h) / \int_0^{h_{\text{max}}} dh \cdot L_{\uparrow}(h) \quad (2)$$

From ascertained values of  $H$  and  $E^*$ , we calculate dimensionless elastic strain index  $H/E^*$  and the ratio  $H^3/E^{*2}$  measured in GPa. It is commonly assumed that a material with high  $H/E^*$  ratio like 0.1 possesses a better wear resistance than a material with a low ratio  $H/E^* \sim 0.01$ . Parameter  $H^3/E^{*2}$  controls the resistance of the coating to plastic deformation. Really, to initiate plastic deformation, loading force should exceed the critical value  $L_{\text{cr}} = 0.78 \nu^2 H^3/E^{*2}$  [16]. Therefore, plasticity is reduced

in materials with higher hardness and lower modulus. The next paragraph presents all the above mentioned mechanical parameters measured in BAM films at different loading forces.

### 3.3. Hardness and Young's Modulus

Symbols in Figure 5 present experimental data for hardness  $H$  and Young's modulus  $E^*$  collected for all the indentations made at different loading forces  $L$  in three AlMgB<sub>14</sub> films fabricated within the optimal temperature range 250–350 °C.

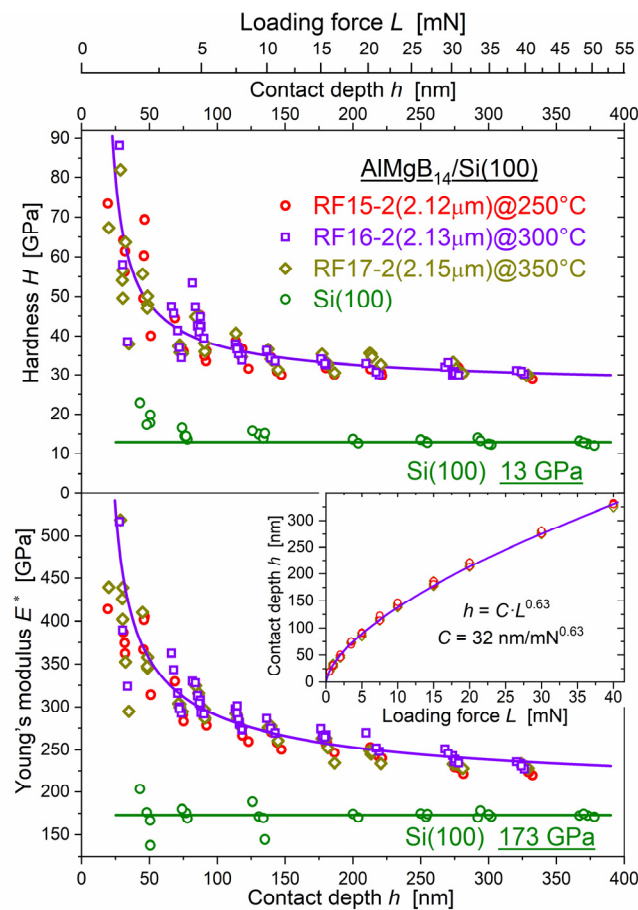


**Figure 5.** Hardness  $H$  and elastic Young's modulus  $E^*$  dependencies upon contact depth  $h$  and loading force  $L$  measured in three different AlMgB<sub>14</sub> films fabricated within the “favorable” temperature range 250–350 °C. Hardness  $H = 13$  GPa and modulus  $E^* = 173$  GPa for a blank single crystal Si(100) wafer are shown for comparison. In inset, solid line is a power law  $h = C \cdot L^{0.63}$  with  $C = 32 \text{ nm/mN}^{0.63}$  fits experimental data for contact depth vs. loading force dependence.

Measurements performed at too shallow notches exhibit severe noise, seem much less reproducible and hence yield big scattering of  $H$  and  $E^*$  data. To find reliable range of the loading force that guaranties authentic results, we have performed the nanohardness test of blank 300  $\mu\text{m}$  thick Si(100) wafer used as a substrate for BAM films deposition (see results are also shown in Figure 5). At loading forces above 2 mN, both measured hardness 13 GPa and Young's modulus 173 GPa are very close to the hardness  $H = 10.5\text{--}13$  GPa and modulus  $E^* = 130\text{--}185$  GPa reported in the literature for different directions in Si single crystals [17–19]. Uncertain values of hardness  $\delta H = 10$  GPa and modulus  $\delta E = \pm 32$  GPa obtained for Si serve as an estimate accuracy of indentation tests at weak loading forces. Despite big scattering of the data observed at shallow indentations, a strong indentation size effect (ISE) is readily seen in Figure 5. Both hardness  $H$  and modulus  $E^*$  sharply increase at weak loads  $L \sim 0.5\text{--}2$  mN (small  $h \sim 20\text{--}50$  nm) reaching the peak values of 88 GPa and 517 GPa, correspondingly. At stronger loading

forces 2–5 mN,  $H$  and  $E^*$  data become less scattered and depth dependent. This “veritable”  $L$  interval starts from 2% and continues to 15% of the relative film thickness indenter’s penetration depth without any indication of Si substrate contribution to  $H$  and  $E^*$ .

### 3.4. Plastic and Elastic Parts of the Indentation Work

In Figure 6, we drew dependencies of the nanohardness  $H$  upon the elastic modulus  $E^*$ , resistance to plastic deformation ratio  $H^3/E^{*2}$  and elastic recovery ratio  $W_e$  vs.  $H$  obtained at different loading forces  $L$ . This plot composed of a complete set of the same, as in Figure 5,  $H$  and  $E^*$  data.

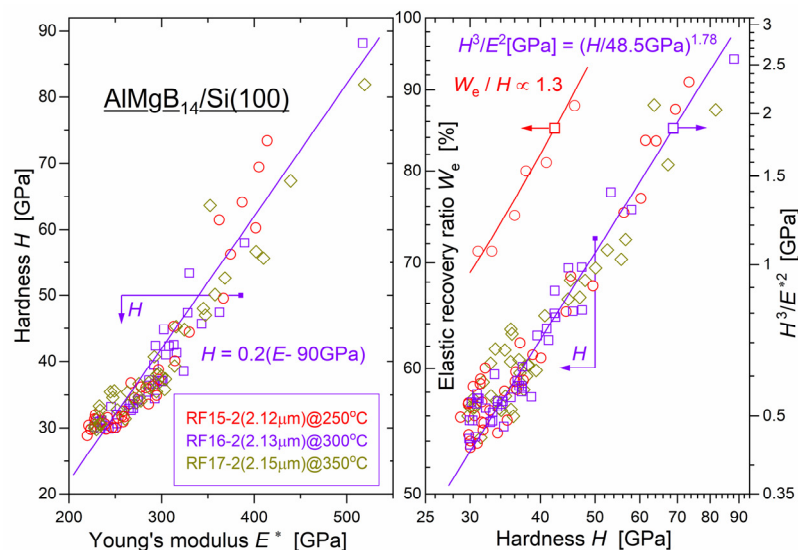


**Figure 6.** Left frame—hardness  $H$  vs. elastic modulus  $E^*$  measured at different loading forces. Right frame—resistance to plastic deformation ratio  $H^3/E^{*2}$  and elastic recovery ratio  $W_e$  vs. hardness  $H$  in the log-log scale.

For all three films grown at “favorable” 250–350 °C temperatures, hardness  $H$  vs. modulus  $E^*$  data form the most dense track along the straight line for which the slope yields high a value of elastic strain index  $H/E^* = 0.2$ . The dependence of resistance to plastic deformation ratio  $H^3/E^{*2}$  upon the nanohardness  $H$  follows the power law  $H^3/E^{*2}[\text{GPa}] = (H/48.5\text{GPa})^{1.78}$ . High hardness is always accompanied with very high values of  $W_e$  growing as  $H^{1.3}$  to become higher than 90%.

When load weakens ( $L < 2$  mN), scattering of  $H$  and  $E^*$  data quickly grows. It happens because the energy dissipating through the plastic deformations suddenly decreases at shallow prints and the shape of load-displacement curves experiences severe distortions. Therefore, the most reliable results for elastic strain index  $H/E^*$  and  $H^3/E^{*2}$  ratio are marked in Figure 6 with the straight lines pointed towards  $H < 50$  GPa. Indentation size effect (ISE) manifests a strong reduction of the main mechanical parameters. It is readily seen in Figures 5 and 6 when the penetration depth of a diamond probe  $h$  increasing from 28 to 330 nm. Namely:  $H$  becomes reduced by 66%,  $E^*$  by 56%, resistance to plastic deformation ratio  $H^3/E^{*2}$  is diminished by 83%, and elastic recovery  $W_e$  decreases from  $90 \pm 5\%$  down to  $71 \pm 1\%$ .

Strong ISE, wide spread of mechanical properties of BAM films and their correlation with hardness resemble results reported by J. Musil for nanocomposite titanium, zirconium and chromium nitride coatings sputtered at different deposition conditions [20,21]. Similar to  $\text{AlMgB}_{14}$ , these films in an amorphous state exhibit superhardness ( $H \geq 40$  GPa), hardness and elastic modulus grow at weak loads whereas energy dissipating through the plastic deformations decreases ( $W_e$  increases up to about 85% for films with  $H \approx 70$  GPa),  $H(L)$  and  $E^*(L)$  values become constant at higher loads  $L$  demonstrating independence on substrate properties. In Figure 6, linear dependence  $H = 0.2(E - 90\text{GPa})$  and power law  $H^3/E^{*2}[\text{GPa}] = (H/48.5\text{GPa})^{1.78}$  obtained for BAM films accord J. Musil’s conclusion on the

general character of these relations for numerous oxides, carbides and nitrides prepared by magnetron sputtering under different deposition conditions [22].

Scratch tests performed with AlMgB<sub>14</sub> films on Si(100) and Corning® 1737 glass substrates enable determination of the second critical loads  $L_{c2}$  when side chips and peelings of coating appear inside the indenter's track. Corresponding  $L_{c2}$  values were used to obtain film-substrate interfacial adhesion strength equal to 18.4 J/m<sup>2</sup> and 6.4 J/m<sup>2</sup> for BAM film on Si(100) and glass substrate, correspondingly (see the details in Ref. [23] and [24]).

#### 4. Conclusions

Optical properties of amorphous magnetron sputtered AlMgB<sub>14</sub> films are characterized by constant in near IR values of refractive index  $n = 2.5$  and extinction coefficient  $k = 0.2$  as well as two bands of Raman-active intra- and inter-icosahedral boron–boron vibrations. Nanoindentation tests displayed a strong indentation size effect (ISE): exceptionally high values of hardness  $H$  and Young's modulus  $E^*$  at the tens-of-nm-scale of indenter penetration depth and a very steep decrease to almost constant parameters at depths which are only 2–3% of films' thickness. Peak values of  $H$  and  $E^*$  correspond to the maximum values of calculated resistance to plastic deformation ratio  $H^3/E^{*2}$  and elastic recovery ratio  $W_e = 90\%$ . We arrived at the conclusion that ISE is a natural attribute of anomalous low energy dissipated through the plastic deformations at shallow indenter's prints.

#### 5. Patents

Protective BAM coatings sputtered onto glass exhibit a hardness that is 1.5 times higher than in Gorilla® Glass at loads above 15 mN and up to 5 times higher at low mN-range loads (see Ref. [24] and patents [25,26]).

**Funding:** This research was partially supported within the Ministry of Science and Higher Education of the Russian Federation special assignment (No. 0752-2020-0007/AAAA-A20-120070290151-6).

**Conflicts of Interest:** The funders had no role in the design of the study; in the collection, analyses, or interpretation of data; in the writing of the manuscript, or in the decision to publish the results.

#### Appendix A

To model experimentally recorded optical transmittance spectrum, in Figure 2 we employed a commonly used Swanepoel [9] formula, Equation (A1):

$$T(\lambda) = \frac{A(\lambda)x(\lambda)}{B(\lambda) - C(\lambda)x(\lambda) + D(\lambda)x^2(\lambda)} \quad (\text{A1})$$

Equation (A2) represents the wavelength-dependent coefficients:

$$\begin{aligned} A(\lambda) &= 16s(n^2 + k^2), \\ B(\lambda) &= [(n + 1)^2 + k^2][(n + 1)(n + s^2) + k^2], \\ C(\lambda) &= 2 \cos \phi [(n^2 - 1 + k^2)(n^2 - s^2 + k^2) - 2k^2(s + 1)] \\ &\quad - 2k \sin \phi [(n^2 - s^2 + k^2) + (s^2 + 1)(n^2 - 1 + k^2)], \\ D(\lambda) &= [(n - 1)^2 + k^2][(n - 1)(n - s^2) + k^2], \\ \phi(\lambda) &= 4\pi nt / \lambda, x(\lambda) = \exp(-4\pi kt / \lambda) \end{aligned} \quad (\text{A2})$$

Here  $n(\lambda)$ ,  $k(\lambda)$ , and  $t$  are refractive index, extinction coefficient and thickness of AlMgB<sub>14</sub> film, correspondingly,  $s(\lambda)$  is a substrate refractive index. We built the interpolation formula for the refractive index  $s(\lambda)$  of the Corning® 1737 glass, Equation (A3):

$$s^2 = 1 + \frac{1.252}{1 - (117\text{nm}/\lambda)^2} \quad (\text{A3})$$

For this purpose, we used data for nine wavelengths presented at the vendor website [27]. They indicate 4.6% optical dispersion of the glass refractive index in the concerned range from 300 to 2500 nm.

## References

1. Matkovich, V.I.; Economy, J. Structure of MgAlB<sub>14</sub> and a brief critique of structural relationships in higher borides. *Acta Crystallogr. B* **1970**, *26*, 616–621. [CrossRef]
2. Cook, B.A.; Harringa, J.L.; Lewis, T.L.; Russel, A.M. A new class of ultra-hard materials based on AlMgB<sub>14</sub>. *Scrip. Mater.* **2000**, *42*, 597–602.
3. Higashi, I.; Kobayashi, M.; Okada, S.; Hamano, K.; Lundström, T. Boron-rich crystals in Al-M-B (M = Li, Be, Mg) systems grown from high-temperature aluminum solutions. *J. Cryst. Growth* **1993**, *128*, 1113–1119. [CrossRef]
4. Tian, Y.; Bastawros, A.F.; Lo, C.C.H.; Constant, A.P.; Russell, A.M.; Cook, B.A. Superhard self-lubricating AlMgB<sub>14</sub> films for microelectromechanical devices. *Appl. Phys. Lett.* **2003**, *83*, 2781–2783. [CrossRef]
5. Grishin, A.M.; Khartsev, S.I.; Böhlmark, J.; Ahlgren, M. Ultra-hard AlMgB<sub>14</sub> coatings fabricated by RF magnetron sputtering from a stoichiometric target. *JETP Lett.* **2014**, *100*, 680–687.
6. Hunold, O.; Chen, Y.-T.; Music, D.; Persson, P.O.Å.; Primetzhofer, D.; Baben, M.; Achenbach, J.-O.; Keuter, P.; Schneider, J.M. Correlative theoretical and experimental investigation of the formation of AlYB<sub>14</sub> and competing phases. *J. Appl. Phys.* **2016**, *119*, 085307. [CrossRef]
7. Hunold, O.; Keuter, P.; Bliem, P.; Music, D.; Wittmers, F.; Ravensburg, A.L.; Primetzhofer, D.; Schneider, J.M. Elastic properties of amorphous T<sub>0.75</sub>Y<sub>0.75</sub>B<sub>14</sub> (T = Sc, Ti, V, Y, Zr, Nb) and the effect of O incorporation on bonding, density and elasticity (T' = Ti, Zr). *J. Phys. Cond. Matter* **2017**, *29*, 085404.
8. Roberts, D.J.; Zhao, J.; Munir, Z.A. Mechanism of reactive sintering of MgAlB<sub>14</sub> by pulse electric current. *Int. J. Refract. Met. Hard Mater.* **2009**, *27*, 556–563. [CrossRef]
9. Swanepoel, R. Determination of the thickness and optical constants of amorphous silicon. *J. Phys. E Sci. Instrum.* **1983**, *16*, 1214–1222. [CrossRef]
10. Werheit, H.; Filipov, V.; Kuhlmann, U.; Schwarz, U.; Armbrüster, M.; Leithe-Jasper, A.; Tanaka, T.; Higashi, I.; Lundström, T.; Gurin, V.N.; et al. Raman effect in icosahedral boron-rich solids. *Sci. Technol. Adv. Mater.* **2010**, *11*, 023001.
11. Goubeau, J.; Hummel, D. Die Schwingungsspektren verschiedener Borsauerstoffverbindungen. *Z. Physik. Chem. N. F.* **1959**, *20*, 15–33. [CrossRef]
12. Choudhary, R.B.; Pande, P.P. Lubrication potential of boron compounds: An overview. *Lubr. Sci.* **2002**, *14*, 211–222. [CrossRef]
13. Kleiner, K. Material Slicker than Teflon Discovered by Accident. NewScientist, Technology, 21 November 2008. Available online: <https://www.newscientist.com/article/dn16102-material-slicker-than-teflon-discovered-by-accident/> (accessed on 16 September 2020).
14. Music, D.; Kreissig, U.; Chirita, V.; Schneider, J.M.; Helmersson, U. Elastic modulus of amorphous boron suboxide thin films studied by theoretical and experimental methods. *J. Appl. Phys.* **2003**, *93*, 940–944. [CrossRef]
15. Oliver, W.C.; Pharr, G.M. An improved technique for determining hardness and elastic modulus using load and displacement sensing indentation experiments. *J. Mater. Res.* **1992**, *7*, 1564–1583. [CrossRef]
16. Tsui, T.Y.; Pharr, G.M.; Oliver, W.C.; Bhatia, C.S.; White, R.L.; Anders, S.; Anders, A.; Brown, I.G. Nanoindentation and nanoscratching of hard carbon coatings for magnetic discs. *Mater. Res. Soc. Symp. Proc.* **1995**, *383*, 447–452. [CrossRef]
17. Bhushan, B.; Li, X. Micromechanical and tribological characterization of doped single-crystal silicon and polysilicon films for microelectromechanical systems devices. *J. Mater. Res.* **1997**, *12*, 54–63. [CrossRef]
18. Ueda, M.; Lepienski, C.M.; Rangel, E.C.; Cruz, N.C.; Dias, F.G. Nanohardness and contact angle of Si wafers implanted with N and C and Al alloy with N by plasma ion implantation. *Surf. Coat. Technol.* **2002**, *156*, 190–194. [CrossRef]

19. Hopcroft, M.A.; Nix, W.D.; Kenny, T.W. What is the Young's modulus of silicon? *J. Microelectromech. Syst.* **2010**, *19*, 229–238. [[CrossRef](#)]
20. Musil, J. Hard and superhard nanocomposite coatings. *Surf. Coat. Technol.* **2000**, *125*, 322–330. [[CrossRef](#)]
21. Musil, J.; Kunc, F.; Zeman, H.; Poláková, H. Relations between hardness, Young's modulus and elastic recovery in hard nanocomposite coatings. *Surf. Coat. Technology* **2002**, *154*, 304–313. [[CrossRef](#)]
22. Musil, J.; Jirout, M. Toughness of hard nanostructured ceramic thin films. *Surf. Coat. Technol.* **2007**, *201*, 5148–5152. [[CrossRef](#)]
23. Grishin, A.M. Abrasion resistant low friction and ultra-hard magnetron sputtered AlMgB<sub>14</sub> coatings. *Mater. Res. Express* **2016**, *3*, 046402. [[CrossRef](#)]
24. Putrolaynen, V.V.; Grishin, A.M.; Rigoev, I.V. Anti-Scratch AlMgB<sub>14</sub> Gorilla® Glass Coating. *Tech. Phys. Lett.* **2017**, *43*, 871–874. [[CrossRef](#)]
25. Putrolaynen, V.V.; Grishin, A.M.; Rigoev, I.V. Method for Fabrication of Wear Resistant Aluminum Magnesium Boride Coating. Patent RU 2677810, 7 March 2017.
26. Putrolaynen, V.V.; Grishin, A.M.; Rigoev, I.V. Method for Fabrication of Transparent Wear Resistant Aluminum Magnesium Boride Coating on the Surface of Transparent Glassy Wares. Patent RU 2680548, 28 December 2017.
27. Corning®1737 AMLCD Glass Substrates. Material Information. Available online: <http://www.vinkarola.com/pdf/Corning%20Glass%201737%20Properties.pdf> (accessed on 16 September 2020).



© 2020 by the author. Licensee MDPI, Basel, Switzerland. This article is an open access article distributed under the terms and conditions of the Creative Commons Attribution (CC BY) license (<http://creativecommons.org/licenses/by/4.0/>).